

Full length article

Enhancing the radiation tolerance of high-entropy alloys via solute-promoted chemical heterogeneities



Zhengxiong Su^{a,1}, Jun Ding^{b,1}, Miao Song^c, Li Jiang^d, Tan Shi^a, Zhiming Li^e, Sheng Wang^{a,*}, Fei Gao^c, Di Yun^a, En Ma^{b,*}, Chenyang Lu^{a,f,*}

^a Department of Nuclear Science and Technology, Xi'an Jiaotong University, Xi'an, 710049, China

^b Center for Alloy Innovation and Design (CAID), State Key Laboratory for Mechanical Behavior of Materials, Xi'an Jiaotong University, Xi'an 710049, China

^c Department of Nuclear Engineering and Radiological Sciences, University of Michigan, Ann Arbor, MI 48109, United States

^d School of Materials Science and Engineering, Dalian University of Technology, Dalian, 116024, China

^e School of Materials Science and Engineering, Central South University, Changsha, 410083, China

^f State Key Laboratory of Multiphase Flow, Xi'an Jiaotong University, Xi'an 710049, China

ARTICLE INFO

Keywords:

Chemical heterogeneities
Interstitial atoms
Chemical short-range order
High-entropy alloys
Radiation

ABSTRACT

High-entropy alloys (HEAs) composed of multiple principal elements have the potential to offer extraordinary radiation resistance. Using NiCoFeCrMn HEA as a model, here we introduce carbon and nitrogen interstitial alloying solutes to impart additional chemical heterogeneities in the form of local chemical order (LCO) and associated compositional variations. Density functional theory simulations reveal the chemical short-range order (CSRO) surrounding carbon and nitrogen atoms. Atomic-resolution chemical mapping of the elemental distribution confirms marked sub-nanometer-scale compositional variations well beyond statistical fluctuations. Irradiation experiments at elevated temperatures demonstrate a remarkable reduction in void swelling by at least one order of magnitude compared to the base HEA without carbon and nitrogen alloying. The underlying mechanism is that the interstitial-solute-induced chemical heterogeneities roughen the lattice as well as the energy landscape, impeding the movements of, and constraining the path lanes for, the normally fast-moving self-interstitials and their clusters. The irradiation-produced interstitials and vacancies therefore recombine more readily, delaying void formation. Our findings indicate that HEAs can be alloyed with other LCO / fluctuation-provoking interstitial or even substitutional elements, and thus open a promising avenue towards highly radiation-tolerant alloys.

1. Introduction

The control of defect dynamics is a grand challenge in the field of materials science, as the evolution of defects can lead to significant changes in materials properties [1]. In particular, defect evolution under irradiation is a critical issue in a wide range of disciplines, such as nuclear energy, aerospace applications, high-energy physics, geology, etc. [2,3]. The substitutional solid solutions in the form of high entropy alloys (HEAs) have unique defect dynamics behavior compared to conventional alloys, and therefore exhibit promising mechanical properties [4–7] and radiation resistance [8–10]. HEAs are loosely defined as alloys containing multi-principal (four or more) alloying elements in relatively high concentrations (5–35 at. %), which allows for a significant increase

of the composition space for the alloy design [11,12]. The superior irradiation tolerance is believed to arise from the severe local lattice distortion, decreased energy dissipation at primary irradiation damage stage and unique defect migration properties during long-term defect evolution [13].

It is well known that the conventional alloys usually contain low amounts of solutes, which results in nearly identical chemical environment in their surroundings. Therefore, it is easy to form nearly chemically homogeneous alloys. In comparison, as the alloy elements in HEAs do not distinguish between solute and solvent, the high concentrations of constituent species can result in chemical heterogeneities. The chemical heterogeneities can be in the form of chemical short-range order (first stage of local chemical order) and associated

* Corresponding author.

E-mail addresses: shengwang@mail.xjtu.edu.cn (S. Wang), maen@xjtu.edu.cn (E. Ma), chenylu@xjtu.edu.cn (C. Lu).

¹ These authors contributed equally to this work.

compositional fluctuations in the short-to-medium range (nearest neighbors and the next couple of atomic shells) [14,15]. Recent studies suggest that chemical heterogeneities can influence the mechanical properties of HEAs by modifying the behavior of line defects through enhancement of pinning of dislocations as well as their cross-slip and multiplication [16–19]. For example, Ding et al. have shown that the distribution of stacking fault energy in NiCoCr is sensitive to the varying degrees of local chemical order (LCO) [20]. Zhang et al. revealed the presence of different degrees of chemical short-range order (CSRO) in NiCoCr with different heat treatment methods using energy-filtered transmission electron microscope (TEM), and found that CSRO led to significant improvement of the mechanical properties [18]. Recently, using advanced aberration-corrected TEM techniques, Chen et al. directly observed the presence of CSRO in NiCoV and found that it increased the strain hardening during tensile deformation [19]. A series of irradiation defects, including dislocation loops, network dislocations and voids, are generated in alloy under irradiation [21]. The formation and evolution of these defects are also closely related to the local chemical environment. However, the LCO-related chemical heterogeneities, before the emergence of any precipitates, have not been fully exploited in tailoring and enhancing the irradiation resistance of HEAs.

In this work, we demonstrate that chemical heterogeneities in HEAs have pronounced effects on the irradiation response and can mitigate radiation damage. Our new strategy is to artificially add chemical heterogeneities, closely spaced with a length scale that is well suited for influencing point defect evolution, to enhance the irradiation tolerance of HEAs. To this end, we exploit interstitial alloying elements (i.e., C and N), which have varying chemical affinities with the five principal elements (i.e., Ni, Co, Fe, Cr and Mn). To be noted, interstitial atoms in conventional metals tend to only play the role of randomly occupying interstitial positions [22–25]. By contrast, in high-entropy alloys, due to the existence of multiple principal elements, the difference in chemical affinity between interstitial and substitutional atoms can lead to a preferential distribution of elements in their neighbors [26,27]. In this study, we used density functional theory (DFT) to simulate the elemental and CSRO distributions surrounding C and N solute atoms, and reveal that the presence of CSRO slows down the diffusion rate of self-interstitial atoms and vacancies. The evolution of radiation-induced interstitials and vacancies was altered as a result, titling the balance in the direction of favoring their recombination to delay incipient damage. With this strategy, we have observed unprecedented enhancement of radiation tolerance and suppression of void formation in HEAs under high-temperature irradiation. These findings suggest that tuning chemical heterogeneities by introducing interstitial solutes provides us with a novel design avenue to enhance radiation tolerance in HEAs by targeted tweaking of defect behavior.

2. Materials and methods

2.1. Alloy preparation

The HEA with interstitial carbon and nitrogen solutes, with nominal composition $\text{Ni}_{19.8}\text{Co}_{19.8}\text{Fe}_{19.8}\text{Cr}_{19.8}\text{Mn}_{19.8}\text{C}_{0.5}\text{N}_{0.5}$ (at. %), was prepared from pure metals, carbon, and FeCrN_2 (as the source of nitrogen) (purity higher than 99.8 wt. %) using a vacuum induction furnace. The as-cast HEA was hot-rolled at 900 °C with a thickness reduction ratio of 50 %, and then heat-treated at 1200 °C for 2 h in an Ar atmosphere. The HEA plate was water-quenched after the heat treatment. The chemical compositions of the resultant bulk alloy were measured using wet-

chemical analysis, as listed in Table 1. Samples machined from the HEA plate were ground using SiC paper (up to # 4000 grit), and then polished using a 0.05 μm alumina polishing solution to eliminate deformation layers resulted from mechanical grinding. “Mirror-like” surfaces were achieved to guarantee reliable results from nano-indentation and irradiation.

2.2. Ion irradiation experiments

The samples were irradiated with 3 MeV Ni^{2+} ions at a fluence of $5 \times 10^{16} \text{ cm}^{-2}$ at 420 °C, 480 °C and 540 °C, respectively. The flux was controlled at $2.8 \times 10^{12} \text{ ions/cm}^2/\text{s}$. A rastered beam was used to ensure the homogeneous ion irradiation. Predicted local dose and implanted Ni ion concentration were calculated using SRIM-2013 in Quick Kinchin-Pease Mode. The displacement threshold energy and binding energy for all the constituent elements are set to 40 eV and 0 eV, respectively [28]. The peak damage corresponded to a damage dose about 50 displacement per atom (dpa) at the depth of 1000 nm.

2.3. Microstructural characterization

The cross-sectional TEM samples were prepared using the focused-ion beam (FIB) lift-out technique using a FEI Scios 2 Dualbeam. A flash electrochemical technique was applied to remove FIB-induced damage caused by the Ga^+ ions bombardment to obtain ultra-thin and clean samples. Flash electrochemical technique was performed at -20 °C in a solution of 4 % perchloric acid and 96 % alcohol at a voltage of 15 V for 0.1 s.

To characterize the voids and dislocation loops, the high-resolution scanning transmission electron microscope (STEM) - bright field (BF) and high-angle annular dark field (HAADF) imaging after irradiation was performed on aberration-corrected STEM (FEI Themis Z) operated at 300 keV. A Cs-corrected S/TEM JEM-ARM300F2 operated at 300 keV was employed for atomic resolution energy dispersive spectroscopy (EDS) mapping. The statistics of irradiation-induced defect clusters were analyzed using an Image J software, starting from 100 nm in depth from the irradiation surface to avoid the strong surface effect. The size of the dislocation loops was counted by measuring their longest axis. The statistical error for voids follows the methods in Ref. [29] and the void swelling value was calculated as the ratio of the volume of detectable voids to the analyzed sample volume [30]. For the analysis of voids, four FIB samples with a total imaged area of $6 \mu\text{m}^2$ in different regions were counted. For the size statistics of CSRO, we have counted at least three regions per sample, with a total area of about 800 nm².

2.4. Simulation methodology

DFT-based Monte Carlo simulations were implemented for NiCoFeCrMn-CN alloys. Four independent supercells of NiCoFeCrMn , containing 180 atoms each, were generated as special quasi-random structure (SQS) [31] as the initial starting points; then 2 C and 1 N atoms were randomly inserted into the octahedral sites as interstitials for each supercell. The temperature employed in the Monte Carlo simulations was 327 °C (600 K). Energy calculations were performed with the Vienna ab initio simulation package (VASP) [32–34] using spin-polarized density-functional theory, with a plane wave cut-off energy of 420 eV. Brillouin zone integrations were performed using Monkhorst-Pack meshes with a $2 \times 2 \times 2$ grid [35]. Projector-augmented-wave (PAW) potentials [34] were employed with the Perdew-Burke-Ernzerhof (PBE) generalized-gradient approximation (GGA) for the exchange-correlation functional [36].

The ab initio molecular dynamics (AIMD) simulations were performed for four types of HEAs: solid-solution (without CSRO) NiCoFeCrMn and NiCoFeCrMn-CN , annealed (with CSRO) NiCoFeCrMn and NiCoFeCrMn-CN . We use the lattice Monte Carlo method to obtain varying degrees of CSRO, and this simulation includes swaps of atom

Table 1
Chemical composition of NiCoFeCrMn-CN alloys.

Elements	Ni	Co	Fe	Mn	Cr	C	N
Atomic (%)	19.64	20.12	17.92	19.67	21.21	0.60	0.83
Weight (%)	20.80	21.40	18.06	19.50	19.90	0.13	0.21

types (only for metallic elements) with the acceptance probability based on the Metropolis–Hastings algorithm [20,37], as shown in Fig. S1.

Four independent supercells for each HEA were studied at 927 °C (1200 K) with a fixed supercell volume, and the temperature was controlled by the Nose–Hoover thermostat. The energy cutoff of 300 eV was used with a single k-point (Γ). Spin polarization was not included, considering that the studied temperature in this experiment was much higher than the materials' Curie temperatures [38]. A single [100] interstitial dumbbell or vacancy was randomly introduced at one of the lattice sites (not close to C and N atoms) to initiate the simulations for interstitial and vacancy diffusions, respectively [39]. The defect structure (interstitial) was first equilibrated over 5 ps, and the diffusion data was then collected from the subsequent 40 ps simulations. By scrutinizing the atomic details, their diffusion coefficients (D), for vacancy and interstitial diffusion, were calculated as $D = \frac{\langle r^2(t) \rangle}{6t}$, where $\langle r^2(t) \rangle$ is the corresponding mean square displacement (MSD).

3. Results

3.1. Design strategy and microstructure

The HEA we designed has a nominal composition of $\text{Ni}_{19.8}\text{C}_{0.19.8}\text{Fe}_{19.8}\text{Cr}_{19.8}\text{Mn}_{19.8}\text{C}_{0.5}\text{N}_{0.5}$ (hereafter referred to as NiCoFeCrMn-CN). The actual chemical compositions of the bulk alloy measured using wet-chemical analysis are listed in Table 1. Fig 1a presents the X-ray diffraction (XRD) pattern, revealing that the NiCoFeCrMn-CN is still a single-phase face-centered cubic (fcc) HEA, just as the base Cantor alloy NiCoFeCrMn (see Fig 1b for its grain structure examined using electron back-scattering diffraction (EBSD) mapping). Fig 1c displays a HAADF image taken with the [110] zone axis and the corresponding fast Fourier transform (FFT) pattern (inset), showing only the normal fcc Bragg spots.

To observe the size and area fraction of CSRO, we have adopted a newly developed method [19]. Fig 2a-b show the HAADF atomic images along the [112] zone axis for NiCoFeCrMn and NiCoFeCrMn-CN, respectively, and the insets show the corresponding FFT patterns. In addition to the fcc diffraction points (yellow circles), some extra diffuse reflections also emerge (one is circled in red). Using this extra disk, we performed an inverse FFT, which lights up the regions of CSRO, as compared for the two alloys in Fig. 2c-d. The size distribution and area fraction of CSRO are shown in Fig. 2e. The average size of CSRO regions in both alloys is about 0.6 nm, but the area fraction of CSRO in NiCoFeCrMn-CN (37 %) is about twice as large as that in NiCoFeCrMn (20 %). Therefore, the previously observed CSRO featuring alternating arrangement of like and unlike species in the fcc HEA [20] is enhanced in the presence of C and N. This tendency is in fact exacerbated by the chemical preference of the interstitial additions, as they have higher affinity with some of the principal elements than others in the HEA, instigating undulation in chemical composition. In particular, C and N

have their own favorable neighbors, as revealed in our Monte Carlo simulations modeling based on a DFT-constructed lattice (see Methods). The analysis of bonds in Fig. 2f indicate obvious chemical ordering, showing preferential (Co, Fe) around C atoms, and increased (Cr, Mn) around N atoms above the sample average. Fig. S2 sums up the principal species in the first and the second nearest neighbor shells, as an indication of the preferable local environment of the interstitial solute. Around either the C or N, the trend is both in the direction towards Ni depletion and Co-enrichment. The detailed distribution data of four independent NiCoCrFeMn-CN configurations after annealing are listed in Table S1 (1st nearest neighbors) and Table S2 (2nd nearest neighbors). In other words, the CSRO is reflected by a change in the atomic fractions in the immediate vicinity of each interstitial solute, away from the nominal sample composition. As such, the chemical composition becomes locally inhomogeneous, favoring contrasting regions (e.g., Ni-depleted next to Ni-enriched) that alternate in space, at a spacing corresponding to the distance between the individual C and N solutes, which is expected to be about 1–3 nm for the current solute concentrations (0.5 at. % C and 0.5 at. % N).

Fig. 3 shows the chemical composition distribution in the NiCoFeCrMn-CN by three-dimensional reconstruction of atom probe tomography (APT), which reveals no apparent carbides and nitrides. Due to up to 50 % of atoms evaporated from the needle tip could be lost during data collection, such that information from tiny ~1 nm CSRO regions would be buried in the noise [11,19,40], the distributions of all elements seem uniform. Therefore, to probe atomic-level chemical heterogeneities, we resorted to atomic-resolution EDS mapping in a high-resolution aberration-corrected scanning transmission electron microscope (STEM). Fig. 4 shows the atomic-resolution HAADF images and the corresponding EDS mapping of the NiCoFeCrMn-CN alloy with the [110] zone axis parallel to the electron beam. These maps reveal that each of the principal elements in this HEA distributes in an inhomogeneous fashion, when interrogated on atomic level. A close examination, as circled in these EDS maps, suggests a number of brighter / dimmer regions that stand out from the surroundings, with an approximate size of 1 nm in diameter and a spacing on the order of 1–3 nm. Further enlarged images of such local regions (inside the bold white circles) are displayed in the down panel. In addition, the line profiles in a (111) plane projected along the [110] zone axis taken from the EDS maps of NiCoFeCrMn (see Fig. S3) and NiCoFeCrMn-CN (see Fig. 4) are shown in Fig. 5. We observe marked undulation (from 2 % to 60 %) compared with NiCoFeCrMn in the atomic concentration of Ni, Co, Fe, Cr or Mn, with peaks and valleys appearing periodically at a spacing of the order of 1 nm. The period of composition variation for NiCoFeCrMn-CN can also be assessed from the spatial autocorrelation length of each species, by using the S parameter analysis [16] (see Fig. 6). The resultant “wavelength” turns out to be consistent with the separation distance between individual interstitial solutes, which is expected to be about 1–3 nm for the 0.5 at. % C and 0.5 at. % N added into the HEA matrix. Taken

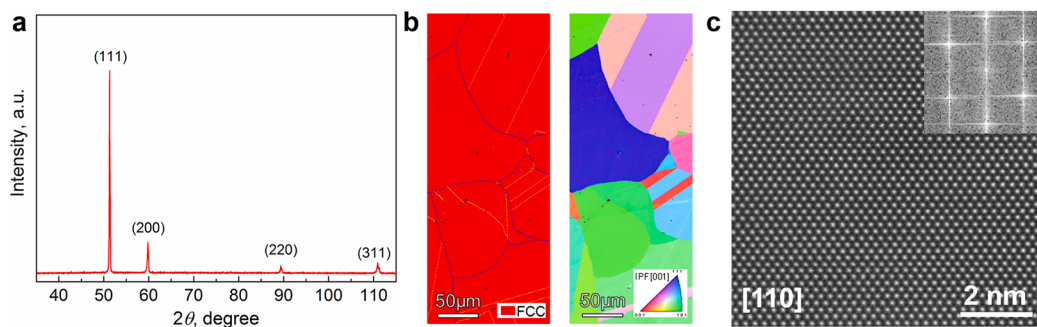


Fig. 1. (a)-(b) XRD pattern and electron back-scatter diffraction maps of the fcc solid-solution NiCoFeCrMn-CN HEA, respectively. (c) HAADF atomic image taken from [110] zone axis and the corresponding FFT pattern (inset).

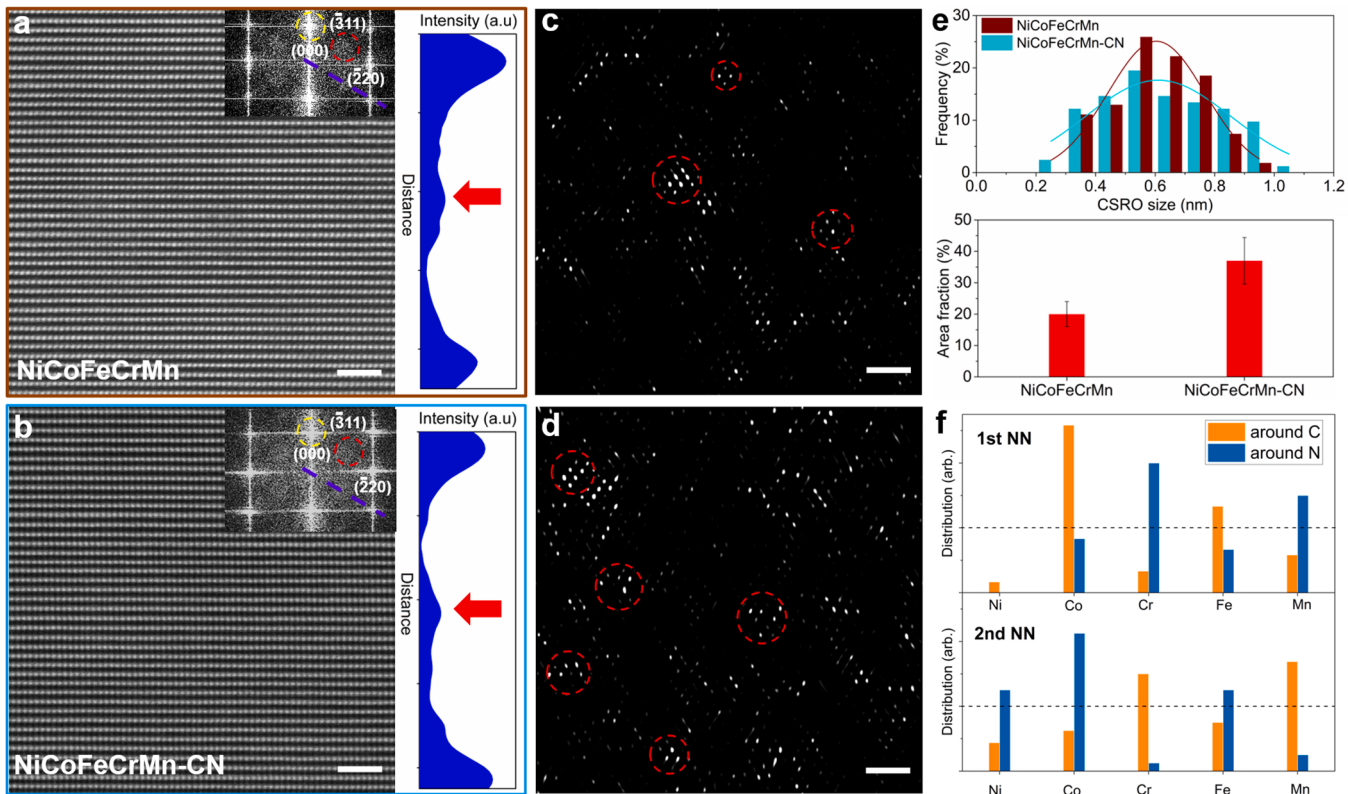


Fig. 2. Characterization of CSRO in NiCoFeCrMn-CN and NiCoFeCrMn. (a) and (b) HAADF atomic image with the [112] zone axis and the corresponding FFT pattern (inset) of NiCoFeCrMn and NiCoFeCrMn-CN, respectively. The yellow circle and red circle in the inset diffraction pattern in the upper right corner, display the Braggs spots from the fcc phase and extra diffuse reflections at 1/2 {311} positions, respectively. Right panel: the intensity of diffraction along the blue dashed line. The red arrows show the intensity at 1/2 {311} positions. All scale bars are 1 nm. (c) and (d) Several CSRO regions are circled in red in the inverse FFT transform from the extra diffuse disk in the FFTs in (a) and (b), respectively. (e) The size and area fraction of CSRO in NiCoFeCrMn and NiCoFeCrMn-CN, based on the inverse FFT images in (c) and (d), respectively. (f) DFT-based Monte Carlo simulation shows the (enriched or depleted) distribution of each principal element around the carbon and nitrogen interstitial solute atoms in their first and second nearest neighbor (NN) shells, deviating from the dashed line corresponding to the concentration level in an ideally homogeneous solid solution.

together, the area fraction of CSRO, the simulated CSRO, and the associated EDS mapping, all point to appreciable chemical inhomogeneity on sub-nanometer scale in NiCoFeCrMn-CN, markedly enhanced over that in the base Cantor alloy without the C- and N- additions.

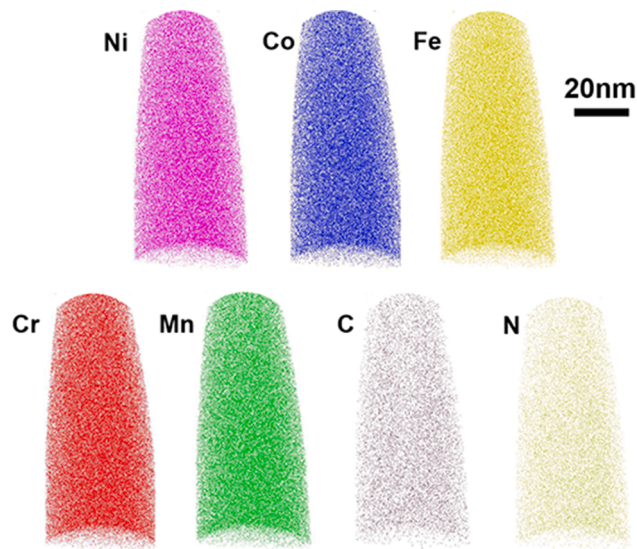


Fig. 3. Three-dimensional reconstructions of a typical atom probe tomography (APT) tip of NiCoFeCrMn-CN.

3.2. Void and dislocation loop evolution

The wide-spread chemical heterogeneities seen in the last section cause variable local atomic bonding environments and therefore affect the evolution of point defects, which in turn alter the evolution of dislocation loops and void swelling. To observe the effect on irradiation response, we performed 3 MeV Ni^{2+} irradiation at several elevated temperatures (420°C , 480°C and 540°C) to a peak dose about 50 dpa. The SRIM-calculated damage and injected ion concentration profiles are also shown in the Fig. 7. We show in Fig. 8 cross-sectional BF TEM images (the BF images were taken under focus to reveal the presence / distribution of voids) of the samples irradiated at the three temperatures. Void formation is absent in the NiCoFeCrMn-CN irradiated at 420°C and 480°C . Apparently, the void is still in the incubation stage at these two relatively low temperatures, where the irradiation-induced free vacancies form stacking fault tetrahedra (SFT) via a vacancy cluster diffusion and agglomeration mechanism [41] (see Fig. S4). In the sample irradiated at a much higher temperature (540°C), some voids show up. Specifically, thermally activated vacancy migration increases with increasing irradiation temperature, such that some vacancies would relocate beyond the predicted damage region, forming small voids in NiCoFeCrMn. In contrast, in NiCoFeCrMn-CN, voids are not observed beyond the ion range at 540°C , and the sparse voids found in the shallow region (< 600 nm) are small and isolated, reflecting the restricted mobility of vacancy clusters to escape from the damage region [42]. It is confirmed that the mobility of vacancy cluster in NiCoFeCrMn-CN is not as pronounced as that of NiCoFeCrMn. Vacancies appear to have a hard time escaping to deeper regions to aggregate into

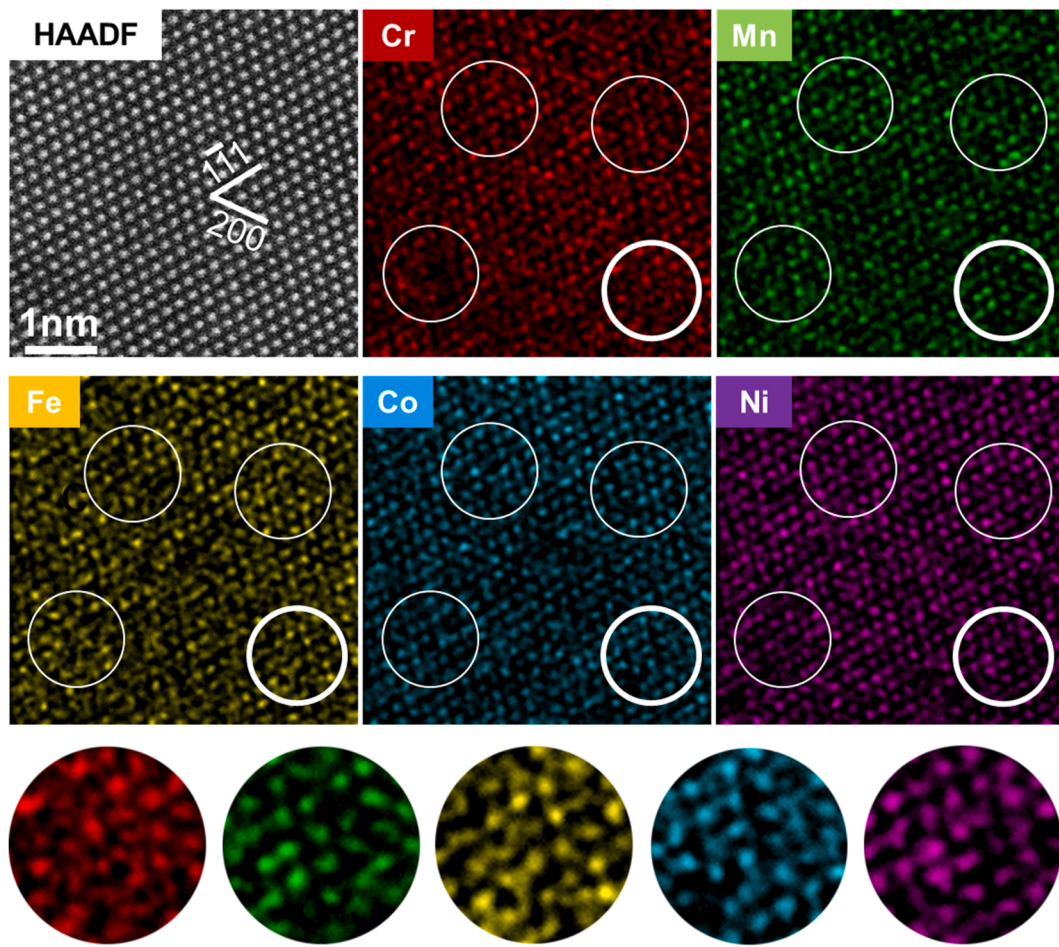


Fig. 4. Elemental distributions in the NiCoFeCrMn-CN HEA. STEM-HAADF image of atomic structure, taken with the [110] zone axis parallel to the electron beam, and corresponding atomic-resolution EDS mapping for individual principal element Ni, Co, Fe, Cr, and Mn. The white circles highlight some brighter / dimmer sub-nanometer regions, with an enlarged view of a local region (inside the bold white circle) displayed in the bottom panel.

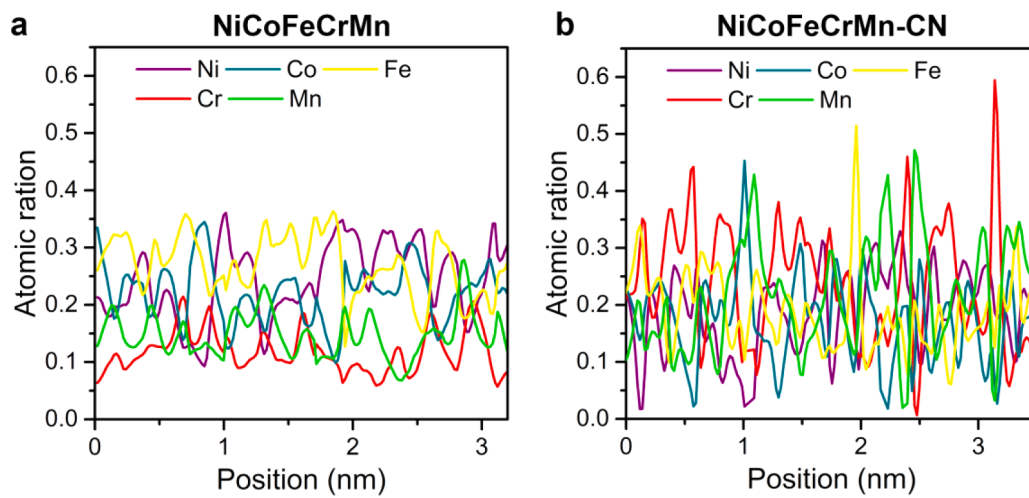


Fig. 5. (a)-(b) Line profiles of atomic fraction of individual elements of NiCoFeCrMn and NiCoFeCrMn-CN taken from the respective EDS mapping, respectively. Each line profile represents the distribution of an element in a (111) plane projected along the [110] zone axis.

voids, which are therefore small, few and far between. The observation that the diffusion distance of vacancies is shorter in NiCoFeCrMn-CN than that in NiCoFeCrMn can be explained by the reduced vacancy migration rate in the presence of C and N, rendering the accumulation of vacancies difficult.

Fig. 9a presents a representative swelling comparison of NiCoFeCrMn-CN and NiCoFeCrMn after irradiation at 420 °C and 540 °C. A striking difference is seen here: with C and N interstitial-solute-induced chemical heterogeneities, the radiation induced swelling seen in NiCoFeCrMn at 420 °C, i.e., the obvious white voids, no longer appear

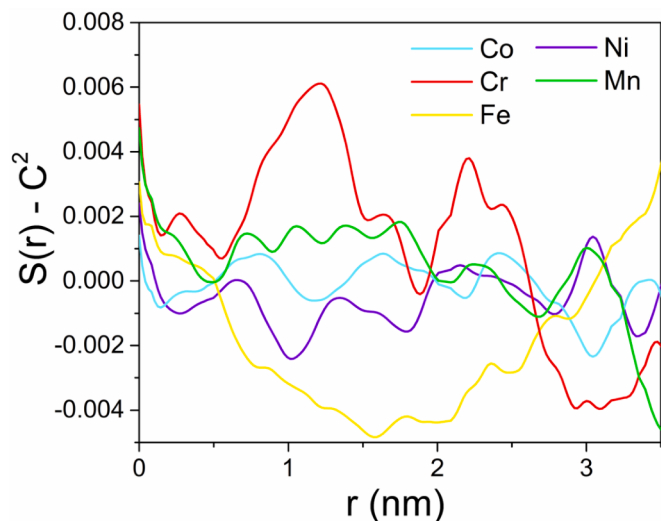


Fig. 6. Plots of pair correlation function $S(r)$ of individual elements of NiCoFeCrMn-CN against concentration wavelength r ; $S(r)$ is shifted by C^2 , where C denotes the average atomic fraction of the corresponding element.

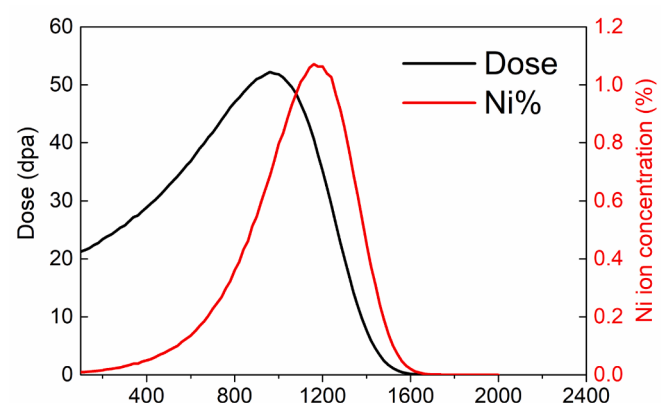


Fig. 7. The depth profiles of damage and implanted Ni concentration calculated for NiCoFeCrMn-CN irradiated with 3 MeV Ni^{2+} ions to a fluence of 5×10^{16} ions/ cm^2 .

in the NiCoFeCrMn-CN. Fig. 9b shows that the overall swelling (0.0009 %) in NiCoFeCrMn-CN is about an order of magnitude lower than that (about 0.008 %) of NiCoFeCrMn, which suggests that NiCoFeCrMn-CN has significantly better swelling resistance than the NiCoFeCrMn. The onset of void formation has been significantly delayed to much higher irradiation temperatures. Moreover, both void growth and swelling are dramatically suppressed. The degrees of void swelling of some typical conventional fcc alloy and medium / high entropy alloys under similar irradiation conditions are also compared in Fig. 9c [43–47]. All samples were probed with a peak dose about 50 dpa. Obviously, NiCoFeCrMn-CN is far superior to other conventional alloys.

It is worth noting that dislocation loops in the region around the implanted Ni concentration peak at 420 °C exhibit an interesting feature: the loop density is higher and the loop size is smaller, relative to those in NiCoFeCrMn (As shown in Fig. 10). This can be attributed to the marked reduction in the self-interstitial cluster mobility in NiCoFeCrMn-CN as compared to NiCoFeCrMn [44]. We have characterized the radiation-induced segregation (RIS) around the dislocation loop and void to confirm the stability of interstitial C / N atoms after irradiation, as shown on Fig. 11 and Fig. 12, respectively. It can be seen that the trend of elemental segregation at void and dislocation loop is similar. The elements of Fe, Mn and Cr are depleted, but Ni and Co enriched. The reason for this phenomenon is due to the difference in vacancy migration energy among different elements [9,48]. Since the vacancy migration energy of Ni, Co is relatively larger, they tend to be enriched at defects. In addition, the segregation of C / N interstitial atoms was not obvious at the defects. The CSRO was characterized using the same characterization method in irradiated area with a dose of about 30 dpa, as shown in Fig. S5. In conclusion, the CSRO still remains relatively steady after irradiation under the experimental conditions used in this study.

4. Discussion

We now discuss the mechanisms responsible for the unusual defect evolution, particularly the impressive void swelling resistance exhibited by the NiCoFeMnCr-CN alloy. Previously, chemical heterogeneities have been reported to affect the dislocation behavior in HEAs, by increasing the dislocation core energy, pinning dislocations, and promoting their cross-slip and multiplication, which in turn improve the work hardening capability and the ductility of HEAs [15,16,20,49,50]. We project that chemical heterogeneities would also affect the evolution of dislocation loops and thus the radiation response in HEAs. As shown above, chemical heterogeneities in this work are enhanced by adding interstitial solutes that have varying chemical affinity with the constituent

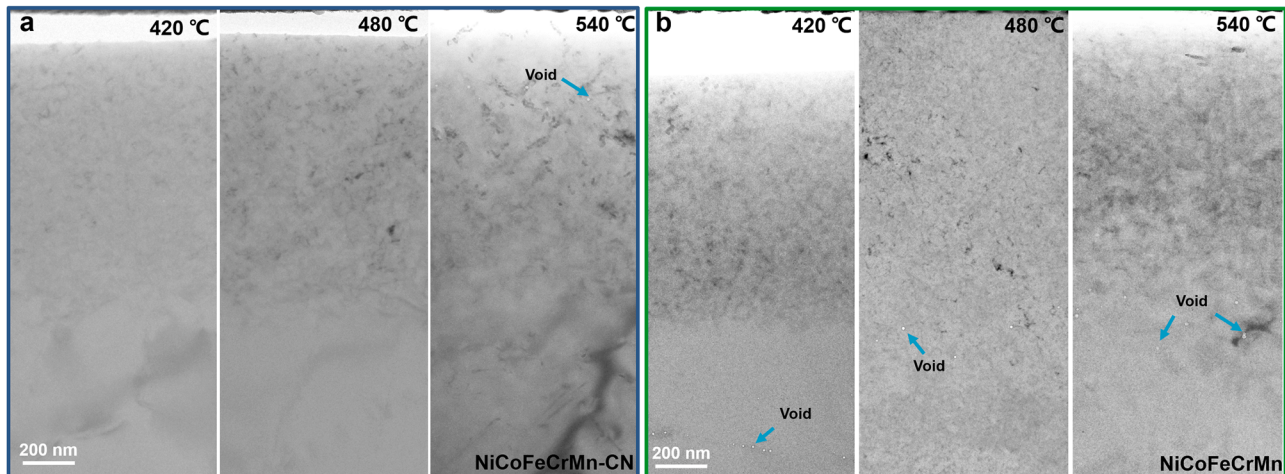


Fig. 8. Distribution of irradiation-induced voids. (a)-(b) Under-focused cross-sectional TEM images in NiCoFeCrMn-CN and NiCoFeCrMn, respectively, irradiated with 3 MeV Ni^{2+} ions at a fluence of 5×10^{16} cm^{-2} at 420 °C, 480 °C, and 540 °C.

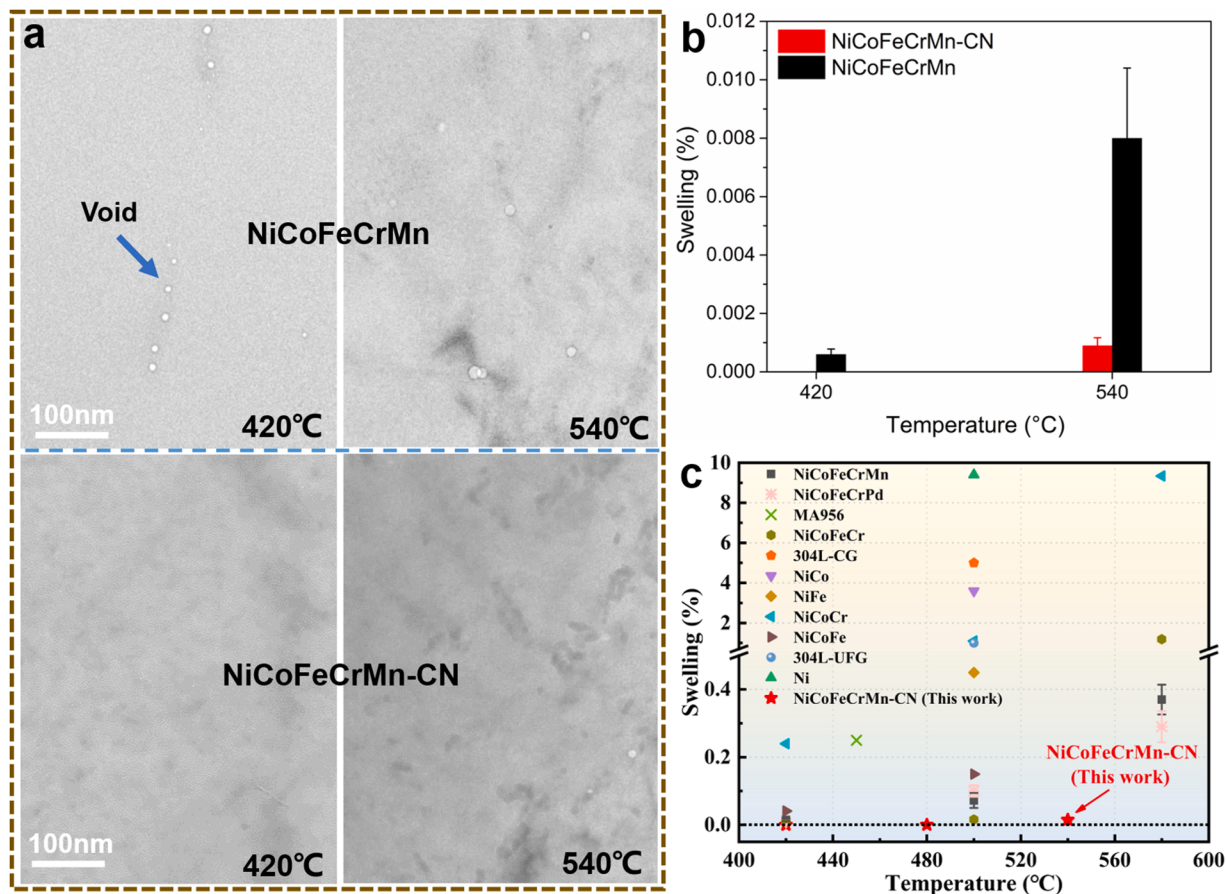


Fig. 9. Comparison of irradiation-induced voids. (a) Under-focused TEM images in NiCoFeCrMn and NiCoFeCrMn-CN, respectively, which have been irradiated with 3 MeV Ni^{2+} ions at a fluence of $5 \times 10^{16} \text{ cm}^{-2}$ at 420 °C and 540 °C. (b) The total void swelling of NiCoFeCrMn versus NiCoFeCrMn-CN. (c) A summary comparing the total void swelling versus irradiation temperature in various alloys [43–47]. All samples were probed with a peak dose about 50 dpa. Some traditional alloys are far inferior to HEAs in their ability to tolerate swelling. The “//” symbol is used to divide the y-axis into two parts to allow a better comparison of the material properties.

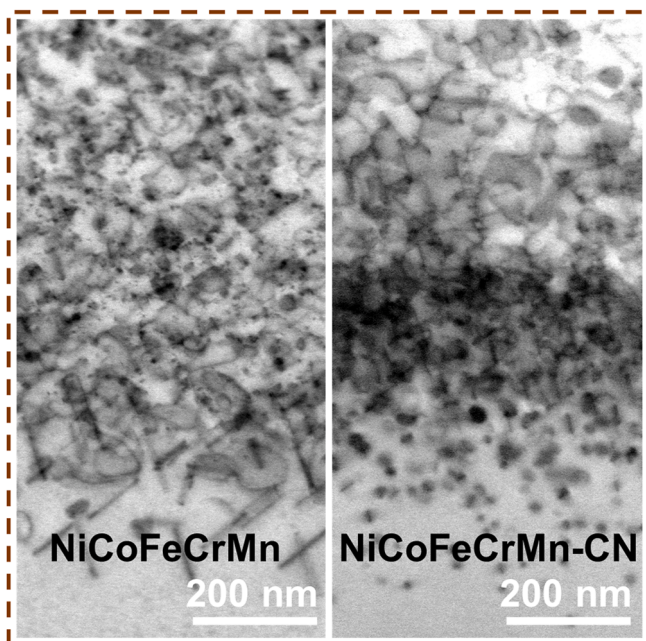


Fig. 10. Comparison of dislocation loops in NiCoFeCrMn and NiCoFeCrMn-CN irradiated at 420 °C in the Ni concentration peak region. STEM-BF image taken from [110] zone axis.

principal elements, leading to CSRO development as incipient LCO, together with associated spatially varying composition on a length scale mostly in the short-to-medium range ($<1.5 \text{ nm}$), before any second-phase precipitates take shape.

The roles played by these chemical heterogeneities are two-fold. First, in the early stage of the irradiation, the chemical heterogeneities can effectively affect electron-phonon coupling to influence the energy dissipation behavior [51–53]. The chemical heterogeneities would reduce the amplitude of d electron hopping in the spin majority channel between the nearest atomic pair [51], thus decreasing the electron mean free path and changing the energy and mass transport properties. Furthermore, the spatial distribution of chemical heterogeneities at the nanoscale causes force variations all the time and all over the place, which give rise to significant phonon scattering and broadening [52]. Both of these phonon and electron effects contribute to the substantial reduction of thermal conductivity in the system, slowing down the dissipation of the deposited heat and prolonging the thermal spike. These effects enhance the defect recombination and disfavor void formation [53].

Second, the chemical heterogeneities reduce the diffusion rates of point defects. On the one hand, the chemical heterogeneities can induce local lattice distortion with associated atomic-level stress field fluctuations. Zhang et al. have shown that, according to their EXAFS analysis, the local lattice distortion in NiCoCr derives mainly from the LCO-induced preferable bonding between certain atomic pairs rather than from atomic size mismatch [54]. There is no doubt that the interstitial C / N atoms can also effectively elevate the lattice strain in high-entropy

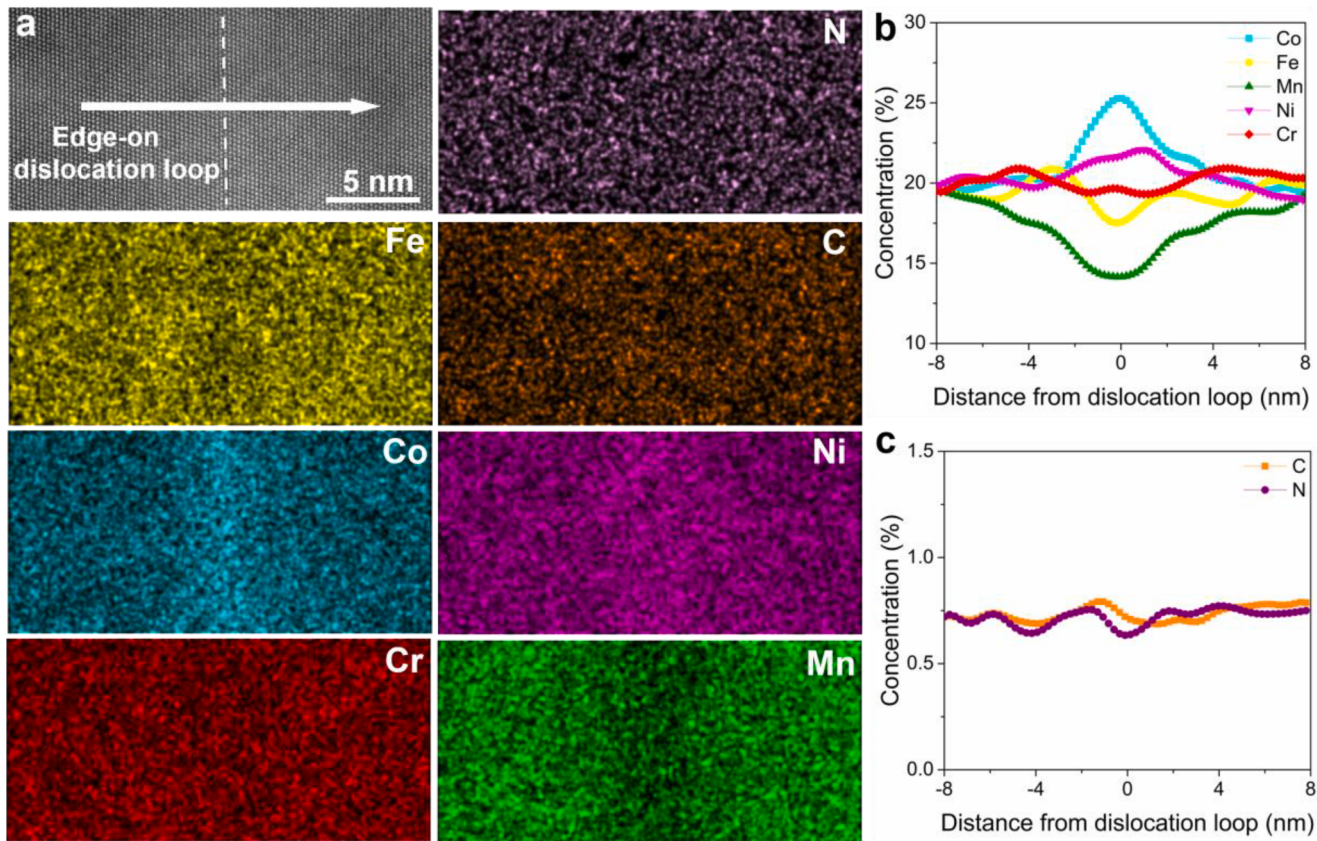


Fig. 11. (a) Radiation-induced segregation near a dislocation loop in NiCoFeCrMn-CN at an irradiation temperature of 420 °C. STEM-HAADF image of an edge-on dislocation loop and the corresponding EDS mapping. (b)-(c) The composition profiles around the dislocation loop (along the arrow) from the mapping in (a).

alloys and slow down the migration of self-interstitial atoms and vacancies. The interstitial C / N atoms can also effectively elevate the lattice strain in high-entropy alloys and slow down the migration of self-interstitial atoms. In our simulations shown in Fig. 13a, the self-interstitial diffusion efficiency of NiCoFeCrMn-CN compared to that of NiCoFeCrMn is reduced by 36 %. On top of that, the increased degree of CSRO in NiCoFeCrMn-CN further reduces the interstitial diffusivity by 34 %. As a result of the sluggish diffusion of self-interstitial atoms, all processes in which interstitial atoms participate should be delayed [55], including those during dislocation loop growth [39]. According to the defect reaction model [56], we know that the probability of annihilation between irradiation-induced vacancies and self-interstitials is higher when their diffusion rates are similar, as that affords the best opportunities for them to run into each other and recombine. With the addition of C and N interstitials, the diffusion rate of self-interstitials is slowed down towards that of vacancies, as shown by the simulation results in Fig. 13b. This trend is more pronounced ($D_{vac}/D_{inter} \approx 0.1$) when CSRO is elevated via simulated annealing / aging. As a consequence, the recombination probability of self-interstitial atoms and vacancies is effectively enhanced, which is responsible for the observed reduction in residual defect concentration and void swelling of the irradiated material. This calculation also allows us to quantitatively evaluate the effect of C / N only as interstitial atoms and its induced CSRO on the diffusion of vacancies and interstitials. Compared to NiCoFeCrMn (without CSRO), the diffusion rate of the interstitial atoms in NiCoFeCrMn (with CSRO) is reduced, as well as its D_{vac}/D_{inter} is increased, suggesting that the introduction of CSRO enhances the defect recombination. In addition, the enhancement in the D_{vac}/D_{inter} of NiCoFeCrMn-CN (with CSRO) to NiCoFeCrMn-CN (without CSRO) is more pronounced, compared to the ratio of NiCoFeCrMn (with CSRO) to NiCoFeCrMn (without CSRO), which also agrees with our claim that the CSRO introduced by the interstitial C / N atoms is more significant and therefore leads to

enhanced defect recombination.

Next, we explain why the migration path of self-interstitial clusters gets strongly altered due to the local chemistry variations [57]. The interaction between CSRO and self-interstitial clusters is schematically shown in Fig. 14. With increasing CSRO, the atomic and energy landscapes become rougher, making the migration of interstitials and the growth of dislocation loops and voids more difficult. This is because chemical heterogeneities will minimize the local free energy. They thus act like local trapping sites of the moving species, by raising their effective migration energy. Recent studies have revealed that LCO at the nanoscale intensifies the ruggedness of the energy landscape and increases the activation barriers for dislocation motion [49]. Similarly, the ordered chemical heterogeneities are expected to escalate the complexity of the energy landscape encountered by the migrating point defects, which can be effectively affected by local inhomogeneities with length scales far smaller than the extent of local chemical order required to influence the motion of the much longer dislocation lines [49]. As a result of the roughened landscape, easier diffusion paths are interrupted, limiting the mobility of self-interstitials to delay their accumulation and long-distance travel [58]. The self-interstitial clusters thus have more opportunities to meet with and take away irradiation-induced vacancies, delaying the coalescence of the latter and hence void nucleation. From the energy cost perspective, the diffusion of self-interstitial atoms would be locked by C and N and their jumps break the preferred local chemical environments, rendering the local environment akin to “antiphase boundary”. This incurs an energy penalty on the migration action, as depicted in Fig. 13a. In particular, the diffusion of self-interstitial clusters amidst chemical heterogeneities is like navigating a vehicle across a rugged terrain, with frequent changes of direction required to seek the minimum migration energy path, rather than running smoothly as in a conventional solid solution alloy.

In this context, the nanoscale chemical heterogeneity is akin to the

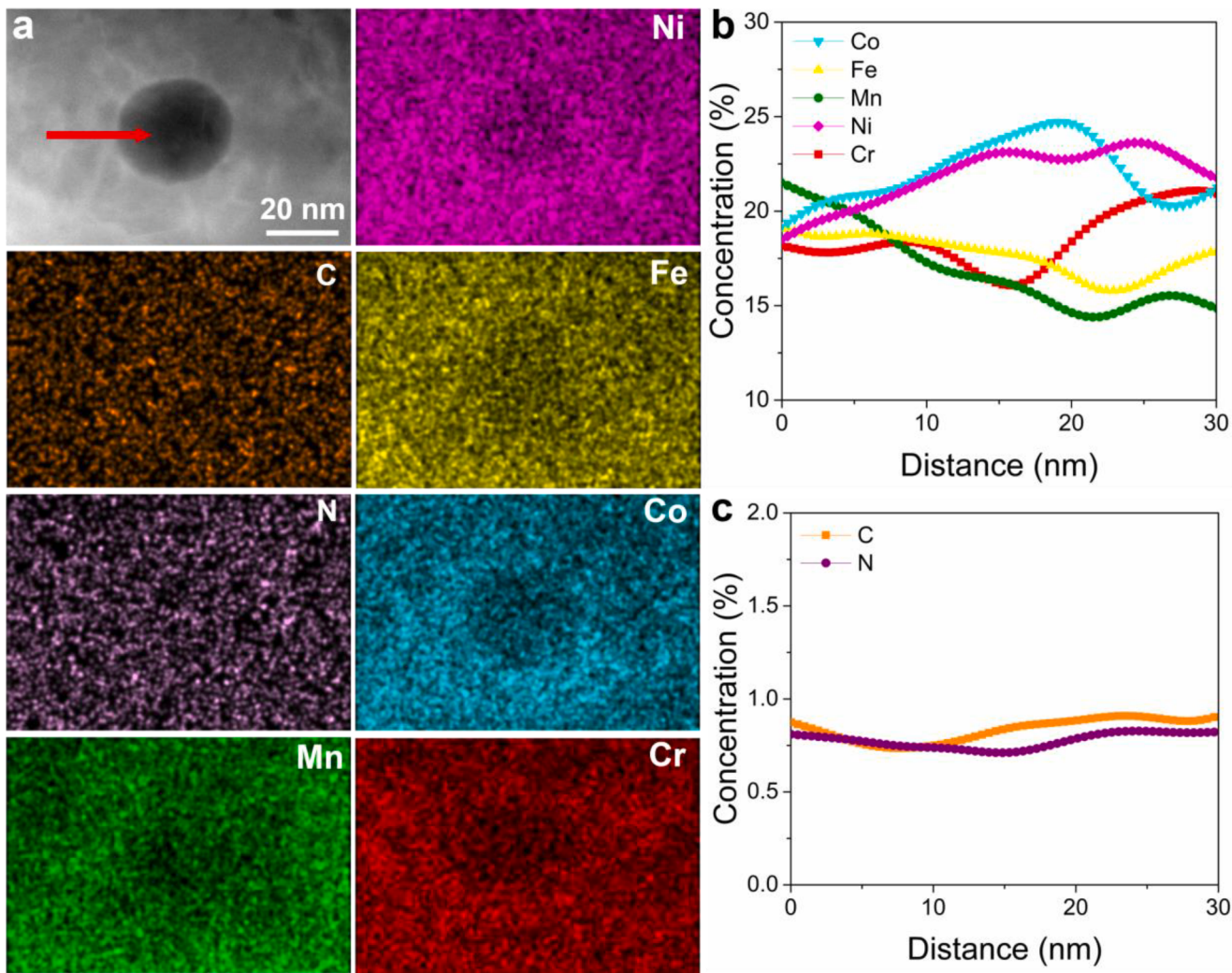


Fig. 12. (a) Radiation-induced segregation near a void in NiCoFeCrMn-CN at an irradiation temperature of 540 °C. STEM-HAADF image of a void and the corresponding EDS mapping. The enrichment of the elements can be seen at the arrow marks. (b)-(c) The composition profiles along the red arrow in (a).

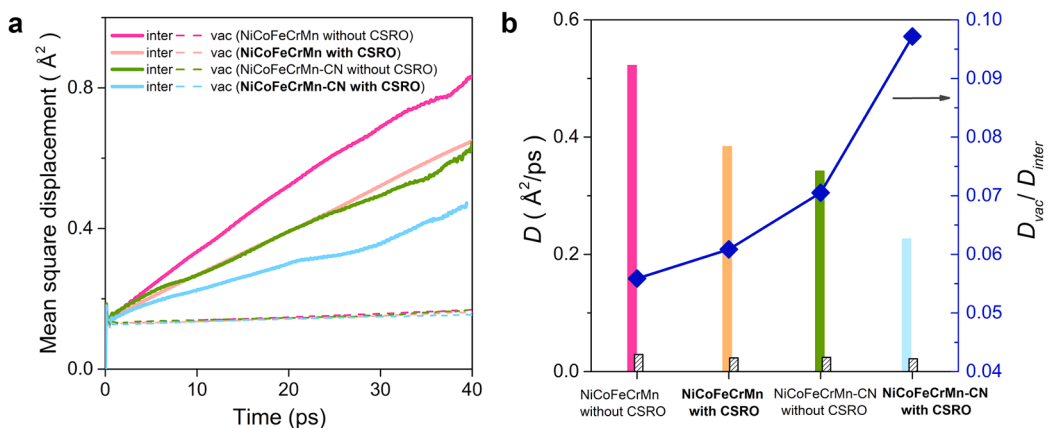


Fig. 13. Chemical short-range order slows down diffusion. (a) The mean square displacement of vacancies and interstitial atoms in NiCoFeCrMn (without CSRO), NiCoFeCrMn (with CSRO), NiCoFeCrMn-CN (without CSRO) and NiCoFeCrMn-CN (with CSRO), respectively. (b) The diffusion coefficients of self-interstitial atoms (D_{inter}) and vacancies (D_{vac}), as well as their ratio.

coherent “precipitates” in the alloy, but a notable difference is that the alloy here remains a single-phase solid solution [17,59]. Recent studies have found that the nanoscale chemical fluctuation could tweak the dislocation slip mode in HEAs from planner slip to wavy slip. The local

chemically ordered (O, Ti, Zr)-structure can act as a tripping and re-routing obstacle for the moving dislocations, leading to frequent cross-slip and dislocation interactions, thereby improving the strain hardening and ductility of $(\text{TiZrHfNb})_{98}\text{O}_2$ alloys [17]. Similar trapping

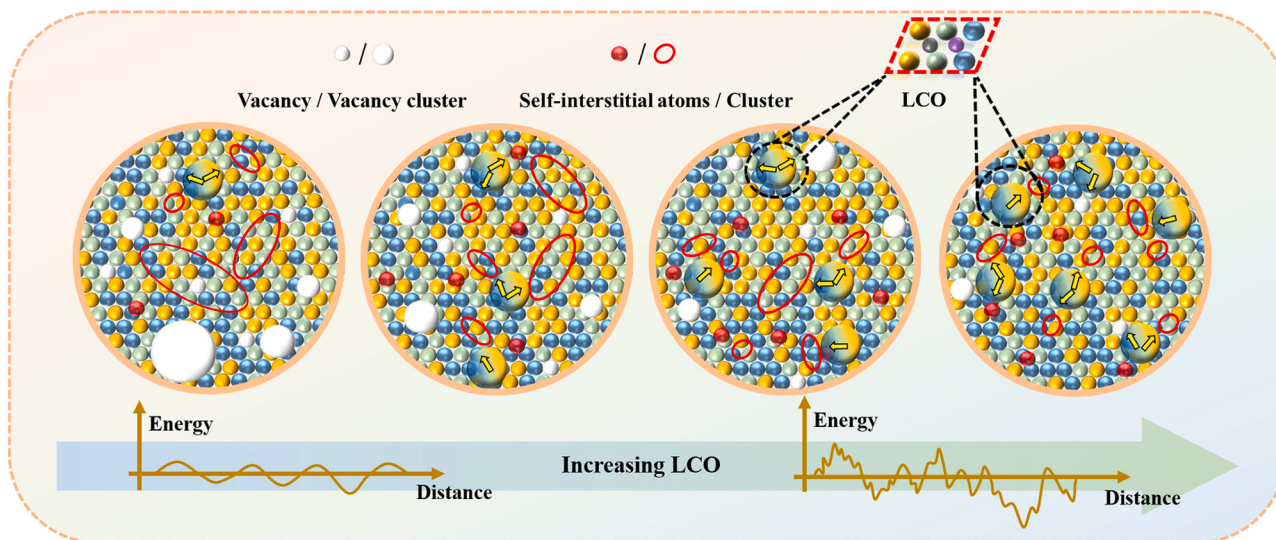


Fig. 14. Schematic illustration of the interplay between LCO and radiation-induced defects in a fcc HEA. The arrows are used to mark the interaction between the migrating point defects and their clusters with LCO, changing their migration trajectory. The bottom schematic illustrates the migration energy landscape confronting the moving defects.

effects have also been seen in NiCoFeCrPd, in which the introduction of Pd brings about a significant nanoscale composition fluctuation [16], slowing down the dislocations. Now that we are dealing with even smaller moving defects, i.e., the radiation-induced self-interstitial clusters, the effective “obstacle / trap” can be even smaller in size, to the point that even CSRO and atomic-scale composition variations will suffice to influence the migration mode of the point defects. Diffusing point defects are expected to be diverted with increasing chemical heterogeneity. As the migration paths are no longer equivalent in all directions due to the variability in the local chemical composition / order, straight-ahead hopping of self-interstitial atoms tends to become “dancing around in circles”. In previous work adopting the multi-principal element recipe [60], we have observed that the migration paths of defects change from random long-range 1D-diffusion to local short-range 3D-diffusion. The *in-situ* experiment confirmed that in a highly concentrated solution, the jump frequency and the glide distance of the dislocation loops were reduced [61], because destroying chemically inhomogeneous structure requires additional energy and generates a local antiphase boundary. By the same token, in NiCoFeCrMn-CN the migration of the radiation-induced defects would be hampered, such that their paths become tortuous and their transport confined in local regions, as depicted in Fig. 14. Certainly, when nuclear structural materials are exposed to irradiation, there are many factors to consider, such as low temperature embrittlement, high temperature oxidation and creep. Therefore, more comprehensive irradiation experiments and mechanical tests are needed in the future to fully evaluate the irradiation resistance behavior.

5. Conclusion

In summary, the present study highlights the power of tailoring chemical heterogeneities as a new strategy to improve the radiation resistance of alloys. We have shown that adding C and N interstitial elements which have varying chemical affinities with the five principal elements in high-entropy alloys elevates chemical short-range order and composition variations, in addition to increasing lattice strain and taking space away from interstitial diffusion channels. The extra chemical heterogeneities raise the barriers against the diffusion of irradiation-induced interstitial atoms and clusters, altering the rates and pathways of these defects in the direction of facilitated recombination with vacancies, thus effectively delaying the void growth and dislocation loop

evolution. These purposely introduced chemical heterogeneities hold promise for rendering alloys with extended service time and expanded operating temperature range, both desirable for the safe operation and energy efficiency of nuclear reactors.

Declaration of Competing Interest

The authors declare that they have no known competing financial interests or personal relationships that could have appeared to influence the work reported in this paper.

Acknowledgements

This work is supported by the National Natural Science Foundation of China under Grant No. 12075179; the National Key Research and Development Program of China under Grant No. 2019YFA0209900. C.L. and E.M. also acknowledge China National Natural Science Foundation (Grant No. 52231001) for supporting this work. We thank JEOL and I. Ohnishi for providing the JEOL-ARM300F2 used for atomic-scale EDS mapping. J.D. and E.M. acknowledges the support of XJTU for their work at CAID. J.D. was supported by the Natural Science Foundation of China (No. 12004294), National Youth Talents Program and the HPC platform of Xi'an Jiaotong University. In addition, we thank Instrument Analysis Center of Xi'an Jiaotong University for characterization.

Supplementary materials

Supplementary material associated with this article can be found, in the online version, at doi:[10.1016/j.actamat.2022.118662](https://doi.org/10.1016/j.actamat.2022.118662).

References

- [1] S.J. Zinkle, G.S. Was, Materials challenges in nuclear energy, *Acta Mater.* 61 (3) (2013) 735–758.
- [2] G.S. Was, D. Pettit, S. Ukai, S. Zinkle, Materials for future nuclear energy systems, *Journal of Nuclear Materials* (2019), 151837.
- [3] B.D. Wirth, How does radiation damage materials? *Science* 318 (5852) (2007) 923–924.
- [4] R. Feng, Y. Rao, C. Liu, X. Xie, D. Yu, Y. Chen, M. Ghazisaeidi, T. Ungar, H. Wang, K. An, P.K. Liaw, Enhancing fatigue life by ductile-transformable multicomponent B2 precipitates in a high-entropy alloy, *Nat Commun* 12 (1) (2021) 3588.
- [5] C. Liu, W.J. Lu, W.Z. Xia, C. Du, Z. Rao, J.P. Best, S. Brinckmann, J. Lu, B. Gault, G. Dehm, G. Wu, Z. Li, D. Raabe, Massive interstitial solid solution alloys achieve near-theoretical strength, *Nat Commun* 13 (1) (2022) 1102.

- [6] Q. Pan, L. Zhang, R. Feng, Q. Lu, K. An, A.C. Chuang, J.D. Poplawsky, P.K. Liaw, L. Lu, Gradient cell-structured high-entropy alloy with exceptional strength and ductility, *Science* 374 (6570) (2021) 984–989.
- [7] T. Yang, Y. Zhao, Y. Tong, Z. Jiao, J. Wei, J. Cai, X. Han, D. Chen, A. Hu, J. Kai, Multicomponent intermetallic nanoparticles and superb mechanical behaviors of complex alloys, *Science* 362 (6417) (2018) 933–937.
- [8] C. Lu, L. Niu, N. Chen, K. Jin, T. Yang, P. Xiu, Y. Zhang, F. Gao, H. Bei, S. Shi, Enhancing radiation tolerance by controlling defect mobility and migration pathways in multicomponent single-phase alloys, *Nat Commun* 7 (2016) 13564.
- [9] Z.X. Su, T. Shi, J.X. Yang, H. Shen, Z. Li, S. Wang, G. Ran, C. Lu, The effect of interstitial carbon atoms on defect evolution in high entropy alloys under helium irradiation, *Acta Mater* 233 (2022), 117955.
- [10] J. Du, S. Jiang, P. Cao, C. Xu, Y. Wu, H. Chen, E. Fu, Z. Lu, Superior radiation tolerance via reversible disordering-ordering transition of coherent superlattices, *Nat Mater* (2022) 1–8.
- [11] E.P. George, D. Raabe, R.O. Ritchie, High-entropy alloys, *Nature Reviews Materials* 4 (8) (2019) 515–534.
- [12] D.B. Miracle, O.N. Senkov, A critical review of high entropy alloys and related concepts, *Acta Mater* 122 (2017) 448–511.
- [13] Y. Zhang, Y.N. Ossetsky, W.J. Weber, Tunable Chemical Disorder in Concentrated Alloys: defect Physics and Radiation Performance, *Chem. Rev.* 122 (1) (2022) 789–829.
- [14] E. Ma, X.L. Wu, Tailoring heterogeneities in high-entropy alloys to promote strength-ductility synergy, *Nat Commun* 10 (1) (2019) 5623.
- [15] E. Ma, Unusual dislocation behavior in high-entropy alloys, *Scr Mater* 181 (2020) 127–133.
- [16] Q.Q. Ding, Y. Zhang, X. Chen, X. Fu, D. Chen, S. Chen, L. Gu, F. Wei, H. Bei, Y. Gao, M. Wen, J. Li, Z. Zhang, T. Zhu, R.O. Ritchie, Q. Yu, Tuning element distribution, structure and properties by composition in high-entropy alloys, *Nature* 574 (7777) (2019) 223–227.
- [17] Z.F. Lei, X. Liu, Y. Wu, H. Wang, S. Jiang, S. Wang, X. Hui, Y. Wu, B. Gault, P. Kontis, D. Raabe, L. Gu, Q. Zhang, H. Chen, H. Wang, J. Liu, K. An, Q. Zeng, T. G. Nieh, Z. Lu, Enhanced strength and ductility in a high-entropy alloy via ordered oxygen complexes, *Nature* 563 (7732) (2018) 546–550.
- [18] R.P. Zhang, S.T. Zhao, J. Ding, Y. Chong, T. Jia, C. Ophus, M. Asta, R.O. Ritchie, A. M. Minor, Short-range order and its impact on the CrCoNi medium-entropy alloy, *Nature* 581 (7808) (2020) 283–287.
- [19] X. Chen, Q. Wang, Z. Cheng, M. Zhu, H. Zhou, P. Jiang, L. Zhou, Q. Xue, F. Yuan, J. Zhu, X. Wu, E. Ma, Direct observation of chemical short-range order in a medium-entropy alloy, *Nature* 592 (7856) (2021) 712–716.
- [20] J. Ding, Q. Yu, M. Asta, R.O. Ritchie, Tunable stacking fault energies by tailoring local chemical order in CrCoNi medium-entropy alloys, *Proceedings of the National Academy of Sciences* 115 (36) (2018) 8919–8924.
- [21] G.S. Was, Fundamentals of Radiation Materials science: Metals and Alloys, Springer, 2016.
- [22] D.J. Hepburn, D. Ferguson, S. Gardner, G.J. Ackland, First-principles study of helium, carbon, and nitrogen in austenite, dilute austenitic iron alloys, and nickel, *Physical Review B* 88 (2) (2013).
- [23] C. Domain, C. Becquart, J. Foct, Ab initio study of foreign interstitial atom (C, N) interactions with intrinsic point defects in α -Fe, *Physical Review B* 69 (14) (2004), 144112.
- [24] Y. Satoh, H. Matsui, T. Hamaoka, Effects of impurities on one-dimensional migration of interstitial clusters in iron under electron irradiation, *Physical Review B* 77 (9) (2008), 094135.
- [25] H. Kim, J.G. Gigax, C.J. Rietema, O. El Atwani, M.R. Chancey, J.K. Baldwin, Y. Wang, S.A. Maloy, Void swelling of conventional and composition engineered HT9 alloys after high-dose self-ion irradiation, *Journal of Nuclear Materials* 560 (2022), 153492.
- [26] Y. Ikeda, I. Tanaka, J. Neugebauer, F. Körmann, Impact of interstitial C on phase stability and stacking-fault energy of the CrMnFeCoNi high-entropy alloy, *Physical Review Materials* 3 (11) (2019), 113603.
- [27] M.Y. He, Y.F. Shen, N. Jia, P.K. Liaw, C and N doping in high-entropy alloys: a pathway to achieve desired strength-ductility synergy, *Applied Materials Today* 25 (2021), 101162.
- [28] R.E. Stoller, M.B. Toloczko, G.S. Was, A.G. Certain, S. Dwaraknath, F.A. Garner, On the use of SRIM for computing radiation damage exposure, *Nuclear Instruments and Methods in Physics Research Section B: Beam Interactions with Materials and Atoms* 310 (2013) 75–80.
- [29] E. Getto, G. Vancoevering, G.S. Was, The co-evolution of microstructure features in self-ion irradiated HT9 at very high damage levels, *Journal of Nuclear Materials* 484 (2017) 193–208.
- [30] T.N. Yang, C.Y. Lu, K. Jin, M.L. Crespillo, Y. Zhang, H. Bei, L. Wang, The effect of injected interstitials on void formation in self-ion irradiated nickel containing concentrated solid solution alloys, *Journal of Nuclear Materials* 488 (2017) 328–337.
- [31] A. Zunger, S.H. Wei, L. Ferreira, J.E. Bernard, Special quasirandom structures, *Phys. Rev. Lett.* 65 (3) (1990) 353.
- [32] G. Kresse, J. Hafner, Ab initio molecular dynamics for liquid metals, *Physical Review B* 47 (1) (1993) 558.
- [33] G. Kresse, J. Hafner, Ab initio molecular-dynamics simulation of the liquid-metal–amorphous-semiconductor transition in germanium, *Physical Review B* 49 (20) (1994) 14251.
- [34] G. Kresse, D. Joubert, From ultrasoft pseudopotentials to the projector augmented-wave method, *Physical review B* 59 (3) (1999) 1758.
- [35] H.J. Monkhorst, J.D. Pack, Special points for Brillouin-zone integrations, *Physical review B* 13 (12) (1976) 5188.
- [36] J.P. Perdew, K. Burke, M. Ernzerhof, Generalized gradient approximation made simple, *Phys. Rev. Lett.* 77 (18) (1996) 3865.
- [37] W.K. Hastings, Monte Carlo sampling methods using Markov chains and their applications, *Biometrika* 57 (1) (1970) 97–109.
- [38] S. Huang, E. Holmström, O. Eriksson, L. Vitos, Mapping the magnetic transition temperatures for medium-and high-entropy alloys, *Intermetallics* 95 (2018) 80–84.
- [39] S. Zhao, Y. Ossetsky, Y. Zhang, Preferential diffusion in concentrated solid solution alloys: NiFe, NiCo and NiCoCr, *Acta Mater* 128 (2017) 391–399.
- [40] L. Zhou, Q. Wang, J. Wang, X. Chen, P. Jiang, H. Zhou, F. Yuan, X. Wu, Z. Cheng, E. Ma, Atomic-scale evidence of chemical short-range order in CrCoNi medium-entropy alloy, *Acta Mater* 224 (2022), 117490.
- [41] D.S. Aidhy, C. Lu, K. Jin, H. Bei, Y. Zhang, L. Wang, W.J. Weber, Formation and growth of stacking fault tetrahedra in Ni via vacancy aggregation mechanism, *Scr Mater* 114 (2016) 137–141.
- [42] A. Barashev, Y. Ossetsky, H. Bei, C. Lu, L. Wang, Y. Zhang, Chemically-biased diffusion and segregation impede void growth in irradiated Ni-Fe alloys, *Current Opinion in Solid State and Materials Science* 23 (2) (2018) 92–100.
- [43] K. Jin, C.Y. Lu, L.M. Wang, J. Qu, W. Weber, Y. Zhang, H. Bei, Effects of compositional complexity on the ion-irradiation induced swelling and hardening in Ni-containing equiatomic alloys, *Scr Mater* 119 (2016) 65–70.
- [44] T.N. Yang, C.Y. Lu, G. Velisa, K. Jin, P. Xiu, Y. Zhang, H. Bei, L. Wang, Influence of irradiation temperature on void swelling in NiCoFeCrMn and NiCoFeCrPd, *Scr Mater* 158 (2019) 57–61.
- [45] C. Sun, S. Zheng, C. Wei, Y. Wu, L. Shao, Y. Yang, K. Hartwig, S. Maloy, S. Zinkle, T. Allen, Superior radiation-resistant nanoengineered austenitic 304 L stainless steel for applications in extreme radiation environments, *Sci Rep* 5 (1) (2015) 1–7.
- [46] T. Chen, H. Kim, J.G. Gigax, D. Chen, C.-C. Wei, F. Garner, L. Shao, Radiation response of oxide-dispersion-strengthened alloy MA956 after self-ion irradiation, *Nuclear Instruments and Methods in Physics Research Section B: Beam Interactions with Materials and Atoms* 409 (2017) 259–263.
- [47] X. Liu, J.G. Gigax, J.D. Poplawsky, W. Guo, H. Kim, L. Shao, F.A. Garner, J. F. Stubbins, Radiation response of a Fe–20Cr–25Ni austenitic stainless steel under Fe²⁺ irradiation at 500 °C, *Materialia* 9 (2020), 100542.
- [48] W.M. Choi, Y.H. Jo, S.S. Sohn, S. Lee, B.-J. Lee, Understanding the physical metallurgy of the CoCrFeMnNi high-entropy alloy: an atomistic simulation study, *npj Computational Materials* 4 (1) (2018) 1–9.
- [49] Q.J. Li, H. Sheng, E. Ma, Strengthening in multi-principal element alloys with local-chemical-order roughened dislocation pathways, *Nat Commun* 10 (1) (2019) 3563.
- [50] S. Chen, Z.H. Aitken, S. Pattamattha, Z. Wu, Z.G. Yu, D.J. Srolovitz, P.K. Liaw, Y. W. Zhang, Simultaneously enhancing the ultimate strength and ductility of high-entropy alloys via short-range ordering, *Nat Commun* 12 (1) (2021) 4953.
- [51] S. Mu, Z. Pei, X. Liu, G.M. Stocks, Electronic transport and phonon properties of maximally disordered alloys: from binaries to high-entropy alloys, *J Mater Res* 33 (19) (2018) 2857–2880.
- [52] F. Körmann, Y. Ikeda, B. Grabowski, M.H.F. Sluiter, Phonon broadening in high entropy alloys, *npj Computational Materials* 3 (1) (2017) 1–9.
- [53] Y.P. Lin, T.F. Yang, L. Lang, C. Shan, H. Deng, W. Hu, F. Gao, Enhanced radiation tolerance of the Ni-Co-Cr-Fe high-entropy alloy as revealed from primary damage, *Acta Mater* 196 (2020) 133–143.
- [54] F. Zhang, S. Zhao, K. Jin, H. Xue, G. Velisa, H. Bei, R. Huang, J.Y.P. Ko, D.C. Pagan, J.C. Neufeind, W.J. Weber, Y. Zhang, Local structure and short-range order in a NiCoCr solid solution alloy, *Phys. Rev. Lett.* 118 (20) (2017), 205501.
- [55] K.Y. Tsai, M.H. Tsai, J.W. Yeh, Sluggish diffusion in Co–Cr–Fe–Mn–Ni high-entropy alloys, *Acta Mater* 61 (13) (2013) 4887–4897.
- [56] O. El Atwani, N. Li, M. Lí, A. Devaraj, J. Baldwin, M.M. Schneider, D. Sobieraj, J. S. Wróbel, D. Nguyen-Manh, S.A. Maloy, Outstanding radiation resistance of tungsten-based high-entropy alloys, *Sci Adv* 5 (3) (2019) eaav2002.
- [57] H. Guan, S. Huang, J. Ding, F. Tian, Q. Xu, J. Zhao, Chemical environment and magnetic moment effects on point defect formations in CoCrNi-based concentrated solid-solution alloys, *Acta Mater* 187 (2020) 122–134.
- [58] Y.W. Zhang, X. Wang, Y.N. Ossetsky, Y. Tong, R. Harrison, S.E. Donnelly, D. Chen, Y. Wang, H. Bei, B.C. Sales, K.L. More, P. Xiu, L. Wang, W.J. Weber, Effects of 3d electron configurations on helium bubble formation and void swelling in concentrated solid-solution alloys, *Acta Mater* 181 (2019) 519–529.
- [59] C. Desgranges, J. Delhommele, Can Ordered Precursors Promote the Nucleation of Solid Solutions? *Phys. Rev. Lett.* 123 (19) (2019), 195701.
- [60] C. Lu, T. Yang, L. Niu, Q. Peng, K. Jin, M.L. Crespillo, G. Velisa, H. Xue, F. Zhang, P. Xiu, Interstitial migration behavior and defect evolution in ion irradiated pure nickel and Ni-xFe binary alloys, *Journal of Nuclear Materials* 509 (2018) 237–244.
- [61] S. Shi, H. Bei, I.M. Robertson, Impact of alloy composition on one-dimensional glide of small dislocation loops in concentrated solid solution alloys, *Materials Science and Engineering: A* 700 (2017) 617–621.